CHEMISTRY OF MATERIALS

pubs.acs.org/cm

Article

Engineering Microstructure of Ultraporous Carbon Aerogels as Advanced H_2 Sorbent Carriers

Ruthradharshini Murugavel, Ali A. Rownaghi, and Fateme Rezaei*

Cite This: *Chem. Mater.* 2024, 36, 8565−8577

Read Online

ACCESS | Metrics & More | Article Recommendations | Supporting Information

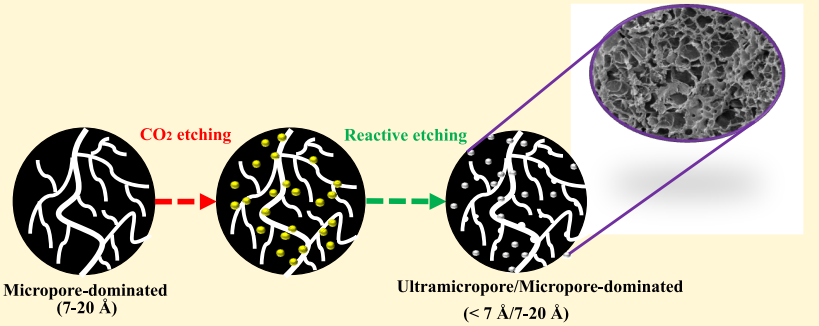

ABSTRACT: In the face of urgent global challenges such as climate change, escalating energy demands, and security concerns, the shift toward sustainable and low-carbon energy is imperative. Hydrogen (H_2), recognized as a versatile and clean energy carrier, holds significant promise as a key facilitator in achieving these objectives. However, H_2 encounters challenges in becoming a reliable energy carrier due to issues related to energy density, ease of storage, and compatibility with existing infrastructure. This paper presents a comprehensive investigation of microstructure engineering in high surface area carbon aerogels to enhance H_2 uptake, addressing a pivotal aspect of H_2 storage applications. We report engineering microstructure of ultramicroporous carbon aerogels via sol−gel and CO_2 supercritical drying methods, as potential H_2 sorbent carriers. Microstructural analysis via N_2, Ar, and CO_2 physisorption measurements revealed that the alteration of microstructure in carbon aerogels through controlled pyrolysis, activation, and pore-forming techniques facilitated the formation of ultramicropores with favorable confinement effects which enhanced intermolecular interactions across the pore walls toward efficient H_2 adsorption. The carbon aerogels, regardless of activation methods, exhibited elevated surface areas between 2970 and 3200 m^2/g and pore volumes in the range of 0.7−1.39 cm^3/g, with a microporous surface area ranging from 950 to 2610 m^2/g. Notably, the double-activated carbon aerogel ($CA_{T20\text{-}F25\text{-}KOH}$) demonstrated the highest H_2 storage capacity of 2.1 wt % and 6.8 g/L under 298 K and 100 bar pressure. At cryogenic temperature (77 K) and 100 bar pressure, $CA_{T20\text{-}F25\text{-}KOH}$ achieved a H_2 storage capacities of 6.8 wt % and 28 g/L. These findings underscore the pivotal role of porosity and surface chemistry in carbon sorbents for H_2 storage.

1. INTRODUCTION

In the quest for a sustainable and environmentally friendly energy future, H_2 has emerged as a compelling contender for the role of a versatile and clean energy carrier. The global community's increasing commitment to mitigating climate change, reducing greenhouse gas emissions, and transitioning away from fossil fuels has accelerated the exploration and adoption of innovative solutions to meet our energy needs. H_2, with its unique properties and potential applications, has captured the imagination of researchers, policymakers, and industry leaders worldwide. Despite the advantage of high energy density (120 MJ/kg), the widespread application of H_2 as a future energy carrier is limited in terms of underlying issues with transportation, storage, and application. Hence, significant progress should be made during the transition to an H_2 fuel economy.

In the past decades, conventional physical storage methods including (i) high-pressure gaseous (HPG), (ii) liquified, and (iii) cryogenic liquefaction storage technologies have suffered from limitations such as low energy density (2.5 wt % and 20 g/L at 400 bar pressure), high energy requirement, boil-off losses, and safety. To satisfy the DOE's (Department of Energy) ultimate targets of 6.5 wt % and 55 g/L,[1] solid-state storage materials such as nanoporous activated carbons (ACs),[2,3] metal−organic frameworks (MOFs),[4,5] and metal hydrides[6] are being studied as they offer high capacity,

Received: February 7, 2024
Revised: July 1, 2024
Accepted: July 2, 2024
Published: July 15, 2024

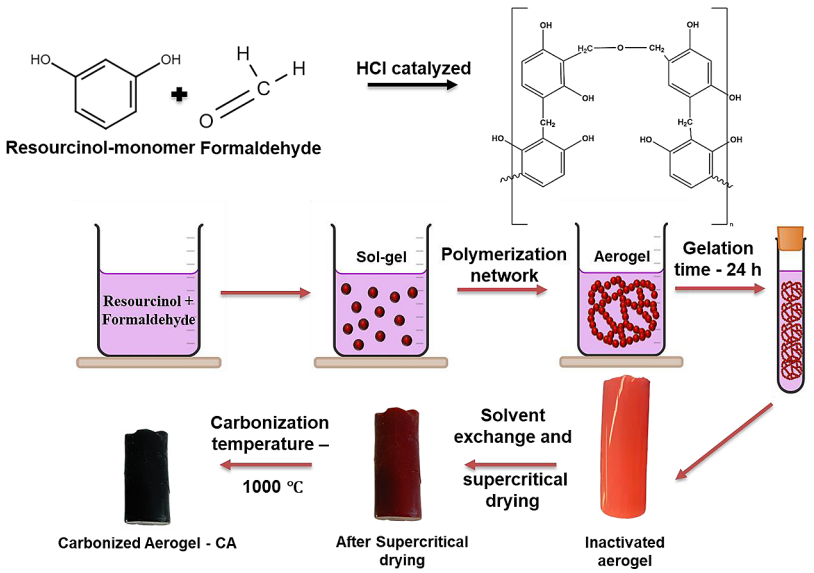

Figure 1. Schematic representation of CAs synthesis.

chemical and structural tunability, fast kinetics, reversibility, and overall efficient and safe storage methods. Among them, physisorption-based materials play a potential role in cryo-adsorption-based storage systems as they tend to reach the ultimate targets for onboard applications.[7,8]

Solid carbon sorbents such as carbon nanotubes,[9−12] fullerenes, nanohorns, aerogels,[13−15] graphite nanofibers,[16,17] zeolite-templated,[18−20] and polymer-derived carbons[2,21−24] are among the well-studied materials due to their high specific surface area and porosity, chemical and structural tunability, and low cost. The H_2 storage capacity of the abovementioned materials typically lies between 1.5 and 6.0 wt % at 77 K, which satisfies the DOE's 2025 system-based target of (5.5 wt %, 40 g/L), considering factors such as weight and volume of the storage system. The interaction between the carbon surface and the H_2 molecules is mostly weak physisorption, and hence, the 77 K adsorption capacity is linear to the surface area (>3000−4000 m^2/g) and micropore volume, as predicted by the Chahine's rule correlation for nanoporous sorbents. Among them, carbon aerogels (CAs) have emerged as a remarkable class of materials from other nanoporous structured sorbents for their wide range of applications including catalyst supports, gas separation and purification, active electrode material for fuel cells, supercapacitors, and H_2 storage.

Aerogels are often referred to as "frozen smoke" or "solid smoke" due to their ultralow density and translucent nature, having a three-dimensional structure of interconnected nanoparticles with characteristic diameters between 3 and 25 nm. This nanostructured framework imparts aerogels with a host of exceptional properties, including an ultrahigh surface area, tunable pore sizes, low density, and thermal insulating capabilities. It is these microstructural attributes that make aerogels an exciting prospect for the efficient adsorption and storage of H_2, a clean and versatile energy carrier crucial to the realization of a sustainable energy future. They are often synthesized using carbonization of template-derived (zeolites, silica, or polymers) method to control their porosity. Another method involves the sol−gel polycondensation of monomers such as resorcinol, phenol, formaldehyde, and others. The solvent extraction is done through supercritical, ambient-pressure, or freeze-drying to reduce the network shrinkage of the gels and, finally, the pyrolysis of the polymerized network to yield a highly porous carbonized aerogel. In general, aerogels are predominantly mesoporous obtained through resorcinol-formaldehyde (RF) polymerized network gels dried through supercritical drying. The fine-tuning of physicochemical and the resulting microstructural properties is achieved through controlling the synthesis conditions such as precursors composition, catalyst type (acid or base), the precursor-to-catalyst ratio, drying procedure, pyrolysis temperature, and other conditions. For example, Pandey et al.[25] studied the effect of initial precursor concentration and the use of an organic catalyst such as triethylamine on the H_2 storage properties RF-based aerogels, which were prepared through the polycondensation of resorcinol with formaldehyde catalyzed by Na_2CO_3 in an aqueous medium.[15] The organic aerogels obtained from the polycondensation reaction consist of a network-like structure formed by interconnected nanosized colloidal-like primary particles. At 77 K, 30 bar, RF-aerogel exhibited an overall uptake of 4.8 wt % that was linearly correlated with the high micropore volume of 0.271 cm^3/g (having a pore size of 1.96 nm).[25] Given the advantages mentioned earlier, developing a CA that can meet the necessary H_2 storage performance metrics remains a challenging task. However, the eventual microstructure network of aerogels is expected to have a high density of ultramicropores having a size range between 3 and 7 Å, which are considered to be the most effective in H_2 storage.[26]

Bearing this background in mind, the main goal of this study was to engineer the ultramicrostructural formation within the aerogel network, based on the optimization of pyrolysis conditions during CO_2 (oxidizing agent) etching. The mechanism adopted is based on the initial oxidative ring fusion aromatization of the phenolic network and the reactive CO_2 etching at higher temperatures to further induce micropore formation.[27] The working hypothesis was that the physical activation promotes the reaction of CO_2 with the heteroatom active sites located on the surface, thus creating ultramicroporosity. We also hypothesized that the decrease in the flow rate of CO_2 would increase the residence time of the etching reaction resulting in the increased probability of CO_2

https://doi.org/10.1021/acs.chemmater.4c00352
Chem. Mater. 2024, 36, 8565−8577

Scheme 1. Reactive Etching Mechanism of Acid-Catalyzed Phenolic Resin-Based Aerogels

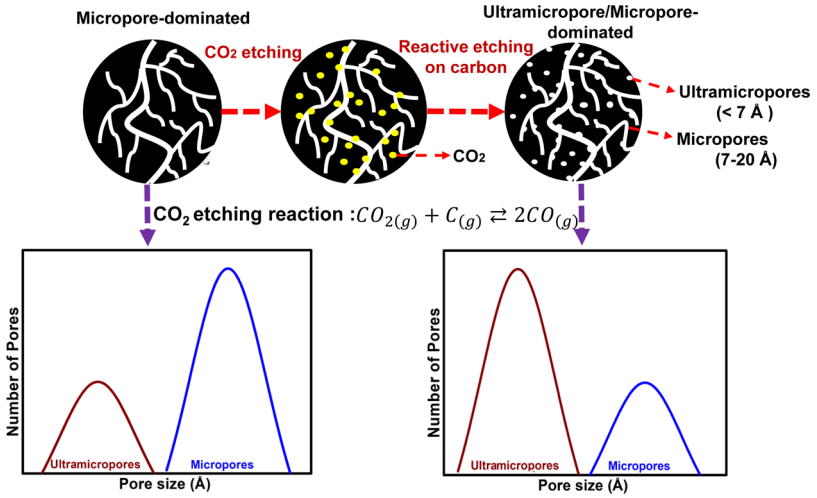

diffusion onto the reaction sites and thus enhancing the overlapping of electrostatic potentials across the ultramicropore walls. On the contrary, an increase in activation time results in the attack of pore walls, thus yielding more mesoporous carbons.[28−30]

The present investigation was based on optimizing the carbonization parameters of CAs as the activation time, CO_2 flow rate, and post-activation conditions to enhance their H_2 storage capacities. It was therefore the purpose of the work to create a balance between the overall specific surface area and ultramicropore volume of the resultant aerogel. The mechanism of pore development as a function of the controlled oxidation reaction rate was studied to gain a better correlation between carbon's microstructural properties and H_2 adsorption. In addition, the high oxygen content on the carbon surface due to the oxidation reaction was determined, and their characteristic effect on the H_2 uptake properties was investigated. The isosteric heat of adsorption was also calculated to determine the strength of interaction between the H_2 molecules on the oxygen-rich carbon surface. Finally, a comparison was drawn between the double-activated and the benchmark porous carbon and the MOF sorbents against the DOE H_2 storage target metrics.

2. EXPERIMENTAL SECTION

2.1. Materials. The following materials were used for sorbent synthesis without further purification: resorcinol, formaldehyde (37% w/w aqueous solution methanol stabilized), acetonitrile (ACS reagent grade), potassium hydroxide (KOH, 99.5%), and hydrochloric acid (HCl-37% N) were purchased from Sigma-Aldrich. Syphon-grade supercritical liquid CO_2, hydrogen (H_2), and ultrahigh purity (UHP) Ar gas were obtained from Airgas.

2.2. Synthesis of Phenolic Resin-Based Aerogels. The synthesis of the phenolic resin-based aerogels described here followed an established procedure upon the previously reported sol−gel polymerization process, as depicted in Figure 1.[27] The polycondensation reaction between phenol or derivatives with formaldehyde results in the phenolic resin product formation.[31] Briefly, resorcinol (0.52 g), acting as the phenolic monomer, was dissolved in 8.09 mL of acetonitrile solvent, while formaldehyde (0.477 mL) was dissolved separately in 4.05 mL of acetonitrile solvent, followed by the addition of 30 μL of concentrated HCl (12.1 N) was as the catalyst. Both the prepared solutions were stirred briefly and poured into polypropylene molds. The molds were then wrapped in parafilm and kept for 24 h at room temperature for gelation and aging. The formed wet gels were washed with acetone (3 × 8 h, using 4 times the volume of the gel each time) and were dried in a supercritical dryer using liquid CO_2 as the supercritical fluid.

2.3. Synthesis of Physically-Activated Carbonized Aerogels. The as-prepared aerogel monoliths were pyrolyzed in a tube furnace under flowing UHP Ar (100 mL/min) at 800 °C for 5 h. After carbonization, the aerogels underwent etching reaction at 1000 °C under flowing CO_2 at prescribed flow rate and time conditions. At the end of the etching period, the cooling was controlled at 2.5 °C/min under continuous Ar flow. During pyrolysis, the complete backbone aromatization yields fused O^+ heteroatomic pyrylium rings along their skeletal framework.[32] The oxidation reaction during CO_2 etching is represented in Scheme 1. The CO_2 molecules diffuse into the aerogel bulk and induce char burnoff on the pore channels and surface, leading to the formation of ultramicropores depending upon the reaction time and flow rate. The optimized etched CA was double activated with $ZnCl_2$ and KOH to further induce microporosity. All the resultant aerogels are labeled and given in Table 1. The synthesis mechanism of etched CA is illustrated in Figure 1.

Table 1. Aerogel Sorbents and Thier CO_2 Etching Conditions

sorbent	CO_2 etching time, flow rate
$CA_{T180\text{-}F300}$	3 h, 300 mL/min
$CA_{T30\text{-}F80}$	30 min, 80 mL/min
$CA_{T20\text{-}F80}$	20 min, 80 mL/min
$CA_{T20\text{-}F50}$	20 min, 50 mL/min
$CA_{T20\text{-}F25}$	20 min, 25 mL/min
$CA_{T20\text{-}F25\text{-}KOH}$	20 min, 25 mL/min-KOH
$CA_{T20\text{-}F25\text{-}ZnCl2}$	20 min, 25 mL/min-$ZnCl_2$

2.4. Synthesis of Chemically-Activated Carbonized Aerogel. The CO_2-activated CA sample, $CA_{T20\text{-}F25}$ synthesized from the above procedure, was further activated with KOH and $ZnCl_2$ as the double-activation agents. During KOH and $ZnCl_2$ activation, precursor-to-carbon mass ratios of 4:1 and 2:1, respectively, were followed. Any increase in the optimized ratios resulted in the pore widening, promoting the formation of a mesoporous structure. The mixture was then heated up to 800 °C at the rate of 2 °C/min for 2 h under N_2 flow for chemical activation. During carbonization, the carbon surface is etched with KOH (oxidizing agent) and $ZnCl_2$ (dehydrating agent), according to the following eqs 1 and 2.

$$6KOH + 2C \rightarrow 2K + 3H_2 + 2K_2CO_3 \quad (1)$$

$$ZnCl_2 + C + H_2O \rightarrow Zn + CO + 2HCl \quad (2)$$

https://doi.org/10.1021/acs.chemmater.4c00352
Chem. Mater. 2024, 36, 8565−8577

The activated sorbents were then washed with 2 M HCl and distilled water until the pH turned neutral and finally dried at 120 °C for 12 h.

2.5. Materials Characterization. N_2, Ar, and CO_2 physisorption isotherms were measured at 77, 87, and 273 K, respectively, on a Micromeritics (3Flex) gas analyzer instrument to determine the textural properties of the sorbents. Before analysis, all samples were degassed at 200 °C under vacuum for 12 h on a Micromeritics Smart VacPrep instrument. Total BET surface areas were determined via the Brunauer−Emmett−Teller (BET) method from the medium-pressure N_2 and Ar physisorption isotherms at 77 K at P/P_0 of 0.995 based on the Gurvich rule by assuming that N_2 has condensed within the pores at this pressure. In addition, the micropore surface area was also obtained from the N_2 and Ar physisorption isotherms by *t*-plot analysis using the Harkins and Jura (H−J) model. The pore size distribution (PSD) was determined from the nonlinear density functional theory (NLDFT) assuming finite slit-shaped pores and a diameter-to-width aspect ratio of 6 in relation to the surface roughness and heterogeneity on the adsorption mechanism. The ultramicropore volume ($V_{\mu p<1.7nm}$) was estimated from the Dubinin−Radushkevich (DR) equation. The micropore volume (V_{micro}—between 1.7 and 2 nm) was obtained from the Barrett, Joyner, and alenda (BJH) method. The mesopore volume (V_{meso}—between 2 and 50 nm), as calculated by $V_T - (V_{\mu p<1.7nm} + V_{micro})$, and total ($\bar{d}_p$) average pore sizes were determined based on volume-weighted average using the NLDFT method. The ultramicropore volume for pores <2 nm was obtained from the CO_2 adsorption data at 1 bar and 273 K using the Horvath−Kawazoe (HK) method. The measurement of skeletal density was determined by a He pycnometer in a Micromeritics AccuPyc II 1340 instrument at room temperature. The aerogel sample surface topographies were assessed using a Hitachi S4700 field-emission scanning electron microscope (FE-SEM). Energy dispersive X-ray spectroscopy (EDS) data were collected from the combination of SEM data and the Genesis software to determine the elemental analysis for the CA sorbents. X-ray photoelectron spectroscopy (XPS) was obtained using a Kratos Axis 165 photoelectron spectrometer using an aluminum X-ray source to excite the samples. To characterize the surface chemistry, the FTIR spectra were collected on a Nicolet FTIR iS50 Model. The graphitic nature of the synthesized CA was also assessed by Raman spectroscopy on a Nicolet-Raman model 550 spectrometer.

2.6. High-Pressure Adsorption Isotherm Measurements. To assess the suitability of the aerogel-derived carbon sorbents to be used as H_2 storage, excess adsorption isotherms of H_2 were obtained at 298 K in the 0−100 bar pressure range on a BELSORP-HP volumetric adsorption analyzer. Before tests, the samples were degassed under vacuum at 300 °C for 12 h. The total adsorption isotherms were then calculated from the excess isotherms that were measured by the instrument using the following eqs 3−7:

$$G_{tot}(P, T)_{grav} = G_{ex}(P, T) + \rho_{gas}(P, T)V_a \tag{3}$$

$$G_{tot}(P, T)_{vol} = G_{ex}(P, T)_{grav}\rho_{bulk} + \rho_{gas}(P, T)V_a \times \Pi \tag{4}$$

$$\Pi = \frac{V_{pore}}{V_{pore} + V_{skel}} = (1 + (\rho_{skel}V_{pore})^{-1})^{-1} \tag{5}$$

$$\rho_{bulk} = \frac{1}{\frac{1}{d_{skl}} + V_p} \tag{6}$$

where $G_{ex}(P, T)$ and $G_{tot}(P, T)$ are the excess and total adsorption capacities (wt %), respectively, V_a is the adsorbed gas film density at room temperature (g/cm^3), V_{pore} is the pore volume of the sorbent (cm^3/g), Π is the interstitial void space or porosity of the sorbent (%), ρ_{skel} and ρ_{bulk} are the skeletal density (cm^3/g) and the bulk density of the sorbent (cm^3/g), respectively, and ρ_{gas} is the density of the H_2 gas (g/cm^3) determined from the NIST database.[33] To calculate the volumetric uptake, the experimentally obtained excess gravimetric adsorption isotherms were multiplied by the bulk density of the sorbent and the film volume obtained at room temperature through Ono−Kondo model, as determined using eq 4. The majority of research studies in the literature have primarily used crystallographic or envelope density to calculate the volumetric capacities of the sorbents.[34] In practical applications, however, it is not possible to pack a storage tank to full capacity of sorbents having a single-crystal density value. This leads to a packing loss of almost 20%; the skeletal density approximation was used to account for the sorbent's skeletal density, the density of H_2 in trapped pores, the interparticle voids, and the dead volume of the sample cell as a result of compression. The empty-cell isotherm was measured before each measurement to subtract from the measured isotherm from the unphysical rise in the gravimetric excess adsorption. Approximately, 0.2−0.5 g of sample was placed in the sample cell of volume 3.02 cm^3 and outgassed at 120 °C for 4−6 h using the built-in Maker's spec Ultimate Vacuum Rotary pump to a pressure of 6.7×10^{-2} Pa (absolute). Using the gas's compressibility factor (*Z*) at each pressure and temperature from the NIST database, the nonideality of the gases was corrected and outgassed at 120 °C for 4−6 h using the built-n Maker's spec Ultimate Vacuum Rotary pump to a pressure of approximately 6.7×10^{-2} Pa (absolute).

2.7. Experimental Determination of the Adsorbed Phase Density. Adsorption of H_2 onto the surface of a porous material occurs when the density profile increases in the vicinity of the pore walls (ideally closer to the density of liquid $H_2 \sim 71$ kg/m^3) and falls to the minimum value equal to the density of the system's bulk gas. Hence, the total amount of gas (G_{abs}) adsorbed within the system was determined, as given in eq 7

$$G_{abs} = G_{ex} + \rho_{gas}V_{film} \tag{7}$$

where G_{abs} (wt %) is the absolute adsorption, ρ_{gas} (g/cm^3) is the real gas phase density, and V_{film} is the adsorbed film volume obtained at cryogenic temperature (cm^3/g). The aforementioned equation substitutes the film volume for the pore volume in the majority of the literature research. However, this pore volume approximation leads to overestimating Δ*H*, as $V_{film} \leq V_{pore}$. Thus, the pore volume was substituted by the saturated adsorbed film volume andV_{film} was determined from the cryogenic temperature adsorption isotherm using the Ono−Kondo model equations, as given in eqs 8 and 9.

$$\left.\frac{dG_{ex}}{d\rho_{gas}}\right|_{\rho_{gas};;=\rho_{film,sat}} = -V_{film} \tag{8}$$

$$G_{ex} = 2a\frac{\left(1 - \frac{\rho_{gas}}{\rho_{film,sat}}\right)\left(1 - e^{E_b/RT}\right)}{1 + \left(\frac{\rho_{film,sat}}{\rho_{gas}} - 1\right)e^{E_b/RT}} \tag{9}$$

where *a* is the scaling factor, $\rho_{film,sat}$ is the saturated film density (g/L), E_b is the binding energy (kJ/mol), and *R* is the universal gas constant (8.314 J/mol·K). The assumptions of the model are based on the density of adsorbed molecules on the slit-shaped pores between the successive polarizing layers. The uptake increases with increasing gas density, saturates, and then declines reaching a linear regime toward the abscissa ($G_{ex} = 0$, $\rho_{gas} = \rho_{film,sat}$), to give the adsorbed film density, $\rho_{film,sat}$. Since the saturation occurs in the high-density regime of $\rho_{gas} >$ 100 g/L, the extrapolation to obtain the slope of the cryogenic adsorption isotherm gives the saturated adsorbed film volume (V_{film}) using the Ono−Kondo fits, as given in eq 8.

2.8. Determination of the Isosteric Heat of Adsorption. The isosteric heat of adsorption (Q_{st}) is a direct measure of the strength of interaction between the solid sorbent and the adsorbate molecules. The common method to determine is based on the Clausius−Clapeyron equation given in eq 10, using the absolute adsorption isotherms (G_{abs}) obtained at three different (close) temperatures at 298, 313, and 328 K.

https://doi.org/10.1021/acs.chemmater.4c00352
Chem. Mater. 2024, 36, 8565−8577

$$Q_{st} = \frac{RT_1T_2}{T_2 - T_1}\ln\frac{P_2}{P_1} \quad (10)$$

The absolute adsorption values were calculated using the experimentally measured excess adsorption (G_{ex}) and the volume of the adsorbed film (as determined from the Ono−Kondo fits in eqs 8 and 9). Thus, it leads to accurate estimations of the binding energy as it involves the assumptions on the film thickness and the potential binding sites irrespective of the temperature change.

3. RESULTS AND DISCUSSION

3.1. General Textural Characterization of Sorbents.

The N_2 physisorption isotherms and PSD profiles of CA sorbents obtained at 77 K are shown in Figure 2, while the

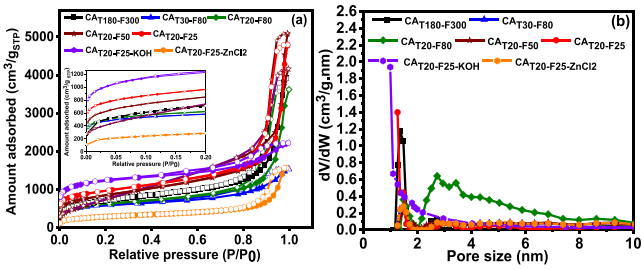

Figure 2. (a) N_2 physisorption isotherms including an inset figure showing the isotherms magnified at low relative pressure region and (b) PSD profiles of CA sorbents.

textural characteristics are outlined in Table 2. According to the IUPAC classification of isotherms, all sorbents showed a combination of type Ia and IVa isotherms with type H1 hysteresis loop, demonstrating their predominant micro-porous-mesoporous structure of the sorbents.[35] The initial steep increase at a very low P/P_0 is characterized by the presence of pore-filling narrow micropores and followed by the saturation plateau at higher relative pressure P/P_0, as shown in Figure 2a. The open hysteresis loop, which is associated with capillary condensation in the narrow mesopores, limits the uptake at high relative pressure.[35] However, the change in the shape of the isotherms suggests the induce of microporosity of the CA sorbents, resulting in the rise in the initial isotherms' elbow at low relative pressure as evident for sorbents such as $CA_{T20\text{-}F25\text{-}KOH}$, as shown in the inset of Figures 2a and S1 in the Supporting Information. The PSD profiles in Figure 2b confirmed the existence of both predominantly micro- and mesopores with an increase in the overall residence time during the etching reaction.

The apparent surface area rose from 2470 m^2/g for sample $CA_{T180\text{-}F300}$ to the highest of 3010 m^2/g for $CA_{T20\text{-}F25\text{-}KOH}$. It should be noted that the sample $CA_{T20\text{-}F25\text{-}KOH}$ has known to surpass the other activated carbons known in the literature in terms of surface area.[7,22,27,36−40] It can be seen that the control sample, $CA_{T180\text{-}F300}$, exhibited a higher surface area than the other sorbents synthesized with a decrease in flow rate and activation time. Though the overall BET surface area decreased, the micropore surface area was found to be enhanced in the order of $CA_{T20\text{-}F25\text{-}KOH}$ (2610 m^2/g) > $CA_{T20\text{-}F25}$ (2100 m^2/g) > $CA_{T20\text{-}F50}$ (1980 m^2/g) > $CA_{T20\text{-}F80}$ (1600 m^2/g) > $CA_{T30\text{-}F80}$ (1450 m^2/g) > $CA_{T180\text{-}F300}$ (1112 m^2/g) > $CA_{T20\text{-}F25\text{-}ZnCl2}$ (950 m^2/g). Thus, it can be concluded that the combined effect of a decrease in flow rate and activation time prolonged the residence time of the overall etching reaction resulting in 89% microporosity, as given in Table 2. The PSD profiles demonstrated a similar upward trend in ultramicropore volume ($V_{\mu p}$) having pore diameter of less than 1.7 nm, with a decrease in mesoporosity of nearly 10%, as listed in Table 2. The increase in ultramicropore volume ($V_{\mu p<1.7\ nm}$) formed at the expense of micropore channel spaces resulted in a reduction in micropore volume ($V_{1.7-2\ nm}$). This change, observed with decreased CO_2 flow rate, signified an improved formation of ultramicropores within the open microporous network, as illustrated in Scheme 1. The increasing order of CA having high ultramicropore volume can be listed as $CA_{T20\text{-}F25\text{-}KOH}$ (1.23 cm^3/g) > $CA_{T20\text{-}F25}$ (0.86 cm^3/g) > $CA_{T20\text{-}F50}$ (0.65 cm^3/g) > $CA_{T20\text{-}F80}$ (0.53 cm^3/g) > $CA_{T30\text{-}F80}$ (0.48 cm^3/g) > $CA_{T180\text{-}F300}$ (0.44 cm^3/g) > $CA_{T20\text{-}F25\text{-}ZnCl2}$ (0.35 cm^3/g), as seen from the rise in initial uptake in the inset of Figure 2a. The optimization of the pyrolysis conditions of the CA sorbents involved the systematic adjustment of flow rate and activation time parameters, which in turn resulted in the $CA_{T20\text{-}F25}$ having a surface area of about 2750 m^2/g and a pore volume of 1.06 cm^3/g, while the control sample ($CA_{T180\text{-}F300}$) exhibited a surface area of 2470 m^2/g and a pore volume of 1.0 cm^3/g. Though the sorbents exhibited comparable BET surface area and total pore volume, the crucial consideration lies in their microporosity, a trend commonly observed in other carbons characterized by lower surface area but higher micropore volume. A possible explanation for this could be due to the limited accessibility of N_2 to infiltrate and diffuse into pores having a size smaller than 2 nm. In addition, factors such as molecular size, diffusion kinetics, and interaction effects with the surface functional groups play a crucial role in surface area

Table 2. Textural Properties of CA Sorbents Based on N_2 Physisorption at 77 K

sorbent	$S_{BET}[S_{\mu p}]$ (m^2/g)[a]	V_{tot} (cm^3/g)[b]	$V_{\mu p(<1.7)}$ (cm^3/g)[c]	$V_{1.7-2nm}$ (cm^3/g)[d]	V_{2-50nm} (cm^3/g)[e]	d_p (nm)[f]	$V_{\mu p}/V_{tot}$ (%)[g]
$CA_{T180\text{-}F300}$	2470[1112]	1.0	0.44	0.2	0.36	1.05	44
$CA_{T30\text{-}F80}$	2098[1450]	0.89	0.48	0.18	0.23	0.99	54
$CA_{T20\text{-}F80}$	1960[1600]	0.85	0.53	0.05	0.27	0.99	62
$CA_{T20\text{-}F50}$	2947[1980]	0.92	0.65	0.22	0.05	0.98	71
$CA_{T20\text{-}F25}$	2750[2100]	1.06	0.86	0.18	0.02	0.99	81
$CA_{T20\text{-}F25\text{-}KOH}$	3010[2610]	1.39	1.23	0.1	0.01	0.97	88
$CA_{T20\text{-}F25\text{-}ZnCl2}$	1800[950]	0.71	0.35	0.23	0.13	1.0	49

[a]First number indicates the BET surface area; the number in the square brackets indicates the micropore area given by the *t*-plot. [b]Single highest volume of N_2 adsorbed in the adsorption isotherm at 77 K (where $P/P_0 \sim 0.997$). [c]$V_{\mu p(<1.7)}$ (ultramicropore volume) was calculated via the DR and NLDFT methods on N_2 adsorption up to 1 bar at 77 K. [d]Micropore volume via BJH. [e]Via $V_{2-50\ nm}$ (mesopore volume) = V_{tot} − ($V_{1.7-2\ nm}$ + $V_{\mu p(<1.7)}$). [f]Average pore width obtained from the NLDFT method. [g]Ratio of micropore volume to the total pore volume of the sorbents pertaining to their microporosity.

https://doi.org/10.1021/acs.chemmater.4c00352
Chem. Mater. 2024, 36, 8565−8577

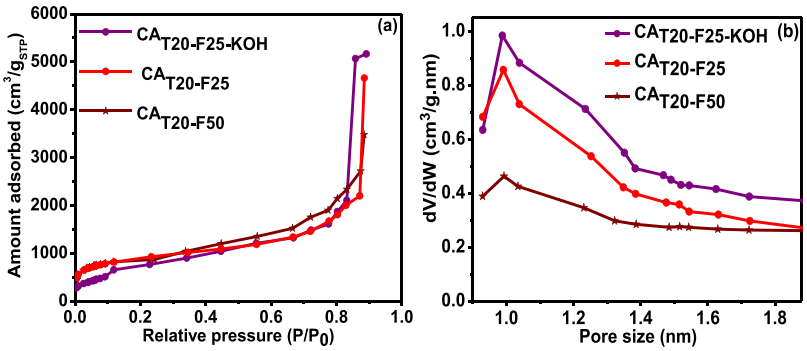

Figure 3. (a) Ar physisorption isotherms and (b) PSD profiles of CA sorbents.

Table 3. Textural Properties of CA Sorbents Based on Ar Physisorption at 87 K

sorbent	$S_{BET}[S_{\mu p}]$ (m^2/g)[a]	V_{tot} (cm^3/g)[b]	$V_{\mu p(<1.7)}$ (cm^3/g)[c]	$V_{1.7-2nm}$ (cm^3/g)[d]	V_{2-50nm} (cm^3/g)[e]	$d_{p\ via\ NLDFT}$ (nm)[f]	$V_{\mu p}/V_{tot}$ (%)[g]
$CA_{T20\text{-}F50}$	2980[1980]	1.12	0.67	0.40	0.05	0.93	59
$CA_{T20\text{-}F25}$	2777[2100]	1.21	0.86	0.18	0.02	0.93	71
$CA_{T20\text{-}F25\text{-}KOH}$	3210[2610]	2.48	1.88	0.1	0.01	0.92	76

[a]First number indicates the BET surface area; the number in the square brackets indicates the micropore area given by the *t*-plot. [b]Single highest volume of Ar adsorbed in the adsorption isotherm at 87 K (where $P/P_0 \sim 0.997$). [c]$V_{\mu p(<1.7)}$ (ultramicropore volume) was calculated via the DR and NLDFT methods on N_2 adsorption up to 1 bar at 77 K. [d]Micropore volume via BJH. [e]Via V_{2-50nm} (mesopore volume) = $V_{tot} - (V_{1.7-300} + V_{\mu p(N2)})$. [f]Average pore width obtained from the NLDFT method. [g]Ratio of micropore volume to the total pore volume of the sorbents pertaining to their microporosity.

estimation. Among the optimized sorbents, $CA_{T20\text{-}F25}$, initially tailored by physical CO_2 activation, was further subjected to chemical activation using agents such as KOH and $ZnCl_2$. The $CA_{T20\text{-}F25\text{-}KOH}$ sample achieved the highest surface area of 3010 m^2/g, surpassing the $CA_{T20\text{-}F25\text{-}ZnCl2}$ surface area of 1800 m^2/g. It can be hypothesized that the KOH activation induced microporosity at the expense of mesopores, compared to $ZnCl_2$[41] on account of the strong base nature and oxidizing properties[41,42] that intercalate the carbon surface and interlayers, thereby promoting the development of ultramicroporous structures. Although the high uptakes at 1 bar based on N_2 adsorption follow the order of $CA_{T20\text{-}F50}$ > $CA_{T20\text{-}F25}$ > $CA_{T20\text{-}F25\text{-}KOH}$, the shape and closing pressure of the hysteresis loop contribute to the increase in total pore volume. For $CA_{T20\text{-}F50}$ and $CA_{T20\text{-}F25}$, the hysteresis shape H1, consisting of cylindrical mesopores, was observed, whereas for $CA_{T20\text{-}F25\text{-}KOH}$, the hysteresis shape H4 over a wide relative pressure range indicated slit-like narrow mesopores with a well-connected network of large micropores. This well-connected structure leads to N_2 uptake over a wide range of pressures, resulting in increased pore volume compared to $CA_{T20\text{-}F50}$ and $CA_{T20\text{-}F25}$.[43] Among the sorbents analyzed in the aforementioned research, the equilibrium balance between their surface area and ultramicropore volume was determined to be in the following order: $CA_{T20\text{-}F50}$ < $CA_{T20\text{-}F25}$ < $CA_{T20\text{-}F25\text{-}KOH}$. Consequently, these three sorbents were selected for further analysis in the study.

The Ar physisorption at 87 K on the three selected sorbents $CA_{T20\text{-}F50}$, $CA_{T20\text{-}F25}$, and $CA_{T20\text{-}F25\text{-}KOH}$ was studied, and the corresponding isotherms are shown in Figure 3a,b. In contrast to N_2, the Ar physisorption isotherms give an accurate determination of their BET surface area and pore size distribution as Ar does not have a quadrupole moment and exhibits fewer specific interactions with surface functional groups. Moreover, since Ar fills narrow pores at significantly higher relative pressures, it leads to accelerated equilibration and permits the measurement of high-resolution adsorption isotherm in a shorter time.[35] Thus, the obtained BET data show 10−15% higher values as listed in Table 3 compared to the BET data obtained from the N_2 adsorption at 77 K. It can be concluded that the Ar adsorption at 87 K would demonstrate to have sufficient adsorbate−adsorbent interactions in obtaining reliable pore size distributions having sizes between 4 and 7 Å. The micropore size distributions were analyzed using the HK slit-shaped pore model for dependable accuracy. The trend for the sorbents for Ar physisorption isotherms showed that the double-activated $CA_{T20\text{-}F25\text{-}KOH}$ exhibited the highest surface area of 3210 m^2/g and total pore volume of 2.48 cm^3/g on account of its ultramicroporous network. The increase in Ar adsorption at higher relative pressure above 0.9 is partly due to the interparticle voids associated with the microstructure of the sample.

The CO_2 adsorption isotherm at 273 K and 1 bar pressure details the narrow ultramicropores, characterized by pores having sizes smaller than 1 nm. Figure 4a,b shows the adsorption isotherms and PSD profiles as determined by the DFT method. The CO_2 physisorption at 273 K facilitates faster diffusion into the narrowest pores than the N_2 physisorption at 77 K. The obtained isotherms were of Type I and showed a sharp rise in the low-pressure region, characteristic of a microporous material according to the IUPAC classification of

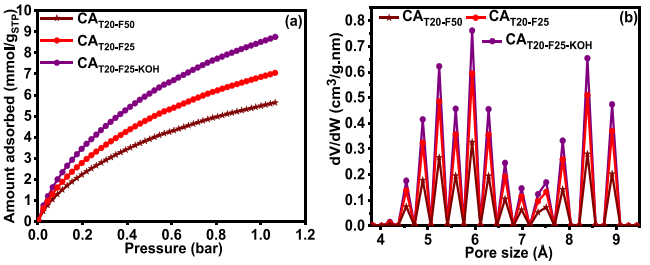

Figure 4. (a) CO_2 adsorption isotherms and (b) PSD profiles of CA sorbents at 273 K and 1 bar.

https://doi.org/10.1021/acs.chemmater.4c00352
Chem. Mater. 2024, 36, 8565−8577

isotherms. The order of the absolute CO_2 uptake can be listed as $CA_{T20\text{-}F25\text{-}KOH}$ (8.9 mmol/g) > $CA_{T20\text{-}F25}$ (7.0 mmol/g) > $CA_{T20\text{-}F50}$ (5.7 mmol/g), which is significantly higher than that over other polymer-derived carbons reported in the literature.[40,44] From the PSD profiles, it was also evident that the sorbents exhibit a large proportion of ultramicropores (3−8 Å) such as $CA_{T20\text{-}F25\text{-}KOH}$ (0.88 cm^3/g) > $CA_{T20\text{-}F25}$ (0.51 cm^3/g) > $CA_{T20\text{-}F50}$ (0.25 cm^3/g). The difference in the ultramicropore volumes across the sorbents is significant considering the hypothetical instrument and methodological error range (15%), as shown in Figure S2 in the Supporting Information. The maximum adsorption capacity was at 8.9 mmol/g, which can be attributed to the surface chemistry and the concentration of functional groups. The proposed interaction mechanism of CO_2 on the surface was due to the increased quadrupole interactions between the pore walls and the heteroatom active sites implied by eq 11. Therefore, it can

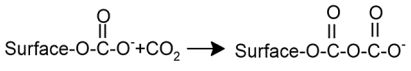

be inferred that the CO_2 isotherm indicates the existence of ultramicropores with sizes smaller than 8 Å. This is in contrast to the cryogenic N_2 and Ar adsorption analysis, which identifies pores larger than 10 Å, as proposed by comparable studies in the literature.[45]

3.2. Structure, Morphology, and Functional Groups of CA Sorbents. The structural properties of the CA sorbents were investigated using an X-ray diffractometer. As shown in Figure 5a, the XRD spectra exhibited two broad peaks centered at 2θ = 22 and 44°, corresponding to the (002) and (100) reflection indices of pristine graphite microstructure. The broad diffraction at 22° is usually considered as the characteristic peak of amorphous carbon. The broad nature of the peaks indicated that the aerogel network was formed by the small carbon particles of the size of ∼5 nm.

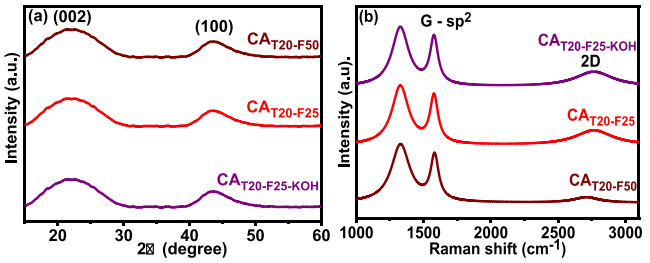

Figure 5. (a) High-resolution XRD patterns and (b) Raman spectra of CA sorbents.

The Raman spectra provide valuable information about the lattice vibration modes of the aerogels, as presented in Figure 5b. The spectra showed two strong D and G peaks centered at 1350 and 1580 cm^{-1}, respectively, associated with the disordering effect and sp^2 hybridized network. The D-band corresponds to the second-order double resonant modes generated from the structural disorder defects in the sp^3 configuration, whereas the G-band represents the C−C bond stretching modes of the sp^2 hybridized network. Moreover, the 2D band at 2656 cm^{-1} contributed to the highly aligned 3D graphitic structure having distinguished layers. The I_D/I_G ratio for the three sorbents was almost in the range of 0.65−1.0, stating the increased level of defects due to the double activation process.[8] The increase in I_{2D}/I_G ratio from 0.44 in $CA_{T20\text{-}F50}$ to 1.0 in $CA_{T20\text{-}F25\text{-}KOH}$ indicated the decrease in the number of graphene layers.[46] It was likely due to the expansion of graphitic multilayers to a few layers, mainly due to KOH intercalation.

The surface morphology of the aerogels was studied via SEM analysis. As with other properties of aerogels, the effect of physical and chemical activation on morphology was investigated. The SEM micrographs of the as-synthesized $CA_{T20\text{-}F50}$, $CA_{T20\text{-}F25}$, and $CA_{T20\text{-}F25\text{-}KOH}$ sorbents are displayed in Figure 6. From the images, it can be concluded that the CA morphology was dominated by the network-like structure of interconnected pores, appearing as voids, channels, and cavities throughout the material. As depicted in Figure 6a−c, it is evident that interparticle gaps resulted in the formation of relatively large pores in $CA_{T20\text{-}F50}$ (a), smaller voids in $CA_{T20\text{-}F25}$ (b), and extremely microsized cavities and thin partitions in $CA_{T20\text{-}F25\text{-}KOH}$ (c). Thus, it can be deduced that lowering the CO_2 flow rate gave rise to the formation of ultramicropores and small cavities (Figure 6e,f), contrasting with the relatively large pores observed upon increasing the flow rate, as depicted in Figures 6d.

The SEM micrograph and the EDS mapping images of the as-synthesized $CA_{T20\text{-}F25\text{-}KOH}$ sample are shown in Figure 7a−d.

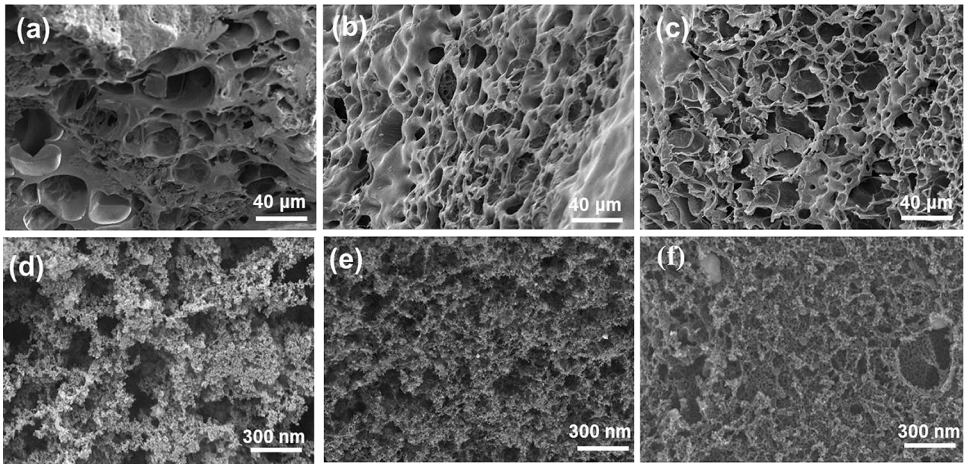

Figure 6. SEM micrographs of (a, d) $CA_{T20\text{-}F50}$, (b, e) $CA_{T20\text{-}F25}$, and (c, f) $CA_{T20\text{-}F25\text{-}KOH}$ sorbents.

https://doi.org/10.1021/acs.chemmater.4c00352
Chem. Mater. 2024, 36, 8565−8577

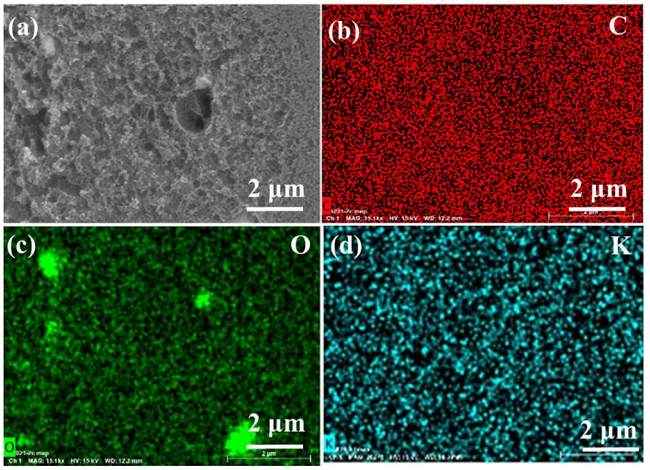

Figure 7. (a) SEM micrograph of $CA_{T20\text{-}F25\text{-}KOH}$ and the corresponding EDS mapping images of (b) C, (c) O, and (d) K elements.

This analysis was performed to assess the elemental composition and distribution on the CA sorbents, which provided a clear evidence for the presence of elemental carbon, oxygen, nitrogen, and potassium, as given in Table S1 in the Supporting Information. The spectra values also showed that the decrease in CO_2 flow rate for sorbents $CA_{T20\text{-}F25}$ and $CA_{T20\text{-}F25\text{-}KOH}$ prolonged the overall oxidation reaction rate, which was evident from the high O content obtained between 18 and 21% in contrast to 4.5% for the $CA_{T20\text{-}F50}$ sample. There was also a decrease in C content which can be due to increased CO_2 diffusion on the reaction sites and the resulting char burnoff. The comparative decrease in oxygen content between $CA_{T20\text{-}F25}$ and $CA_{T20\text{-}F25\text{-}KOH}$ can be due to the KOH activation at high temperatures.

The elemental distributions and their corresponding chemical states were probed via the XPS analysis, as presented in Figure 8. The XPS spectra in Figure 8a show that all three sorbents contained a significant amount of oxygen on their surface on account of the CO_2 etching reaction. The estimated O content was 21% for $CA_{T20\text{-}F25}$, 18.2% for $CA_{T20\text{-}F25\text{-}KOH}$, and 4.5% for $CA_{T20\text{-}F50}$. The relatively lower O content of the $CA_{T20\text{-}F50}$ sample was due to shorter reaction times. The high-resolution spectra further evaluate the chemical states of C 1s at 284.5 eV and O 1s at 531.5 eV for carbon sorbents. Figure 8b shows the C 1s peaks at 284.6 and 285.8 eV, corresponding to the sp^2 hybridized C−C bond and the C−OH bond, respectively.[47] The deconvolution of O 1s at 531.02 and 533.21 eV in Figure 8c revealed the distribution of oxygen functionalities such as the chemically-bonded C=O and C−OH bond, respectively. This is consistent with the O/C ratio stating the relative amounts of C bonded with O listed in Table S1 (Supporting Information). The decrease in O wt % ratio (to the total wt % of all the elements) from 0.26% in $CA_{T20\text{-}F25}$ to 0.22% for the $CA_{T20\text{-}F25\text{-}KOH}$ was due to the reduction reaction on account of the KOH activation.

The functional groups of the optimized CA sorbents were studied using FTIR analysis, as represented in Figure 9. In the shown spectra, the broad peak at 3400 cm^{-1} can be ascribed to the O−H stretching either from the hydroxyl groups bonded to the aromatic ring or physically adsorbed water molecules.

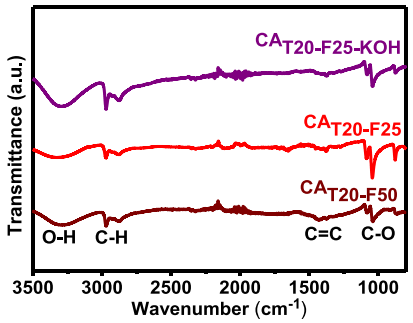

Figure 9. FTIR spectra of as-prepared CA sorbents.

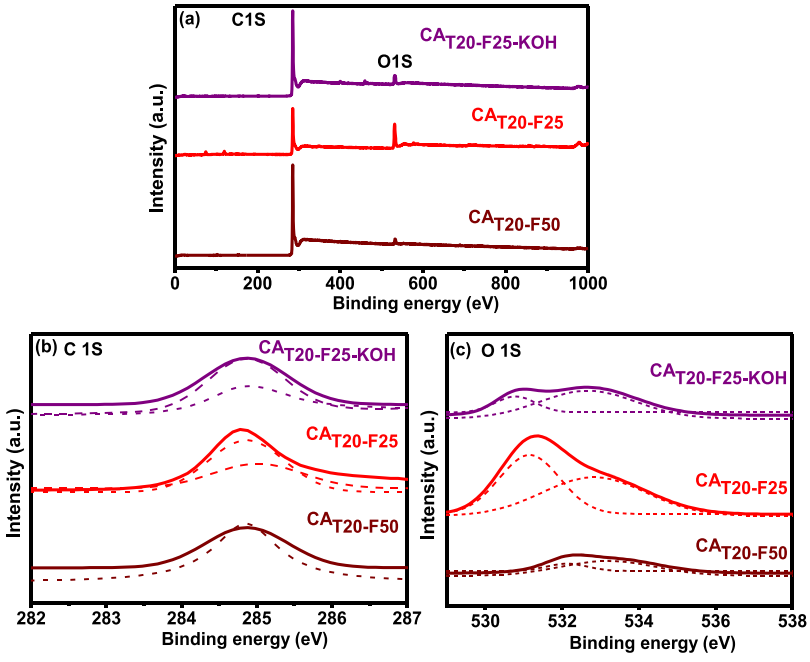

Figure 8. (a) XPS survey spectra and high-resolution XPS spectra of (b) C 1s and (c) O 1s for $CA_{T20\text{-}F50}$, $CA_{T20\text{-}F25}$, and $CA_{T20\text{-}F25\text{-}KOH}$.

https://doi.org/10.1021/acs.chemmater.4c00352
Chem. Mater. 2024, 36, 8565−8577

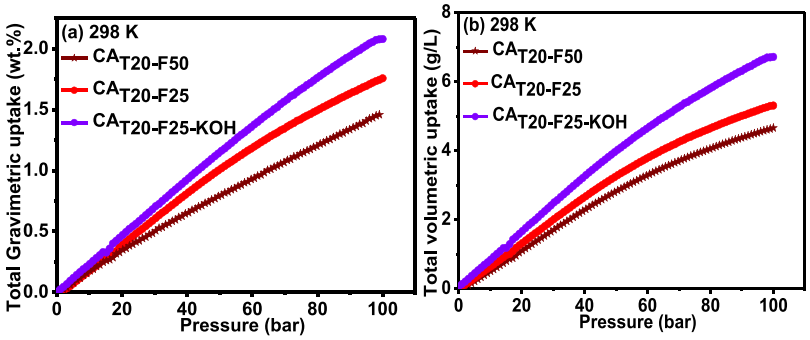

Figure 10. (a) Total gravimetric and (b) volumetric H_2 adsorption isotherms over CA sorbents at 298 K and 0−100 bar pressure range.

C−H stretching peaks were located at 2976 cm^{-1}, and the peaks at 1431 cm^{-1} were associated with the skeleton vibration of aromatic C=C bonds. The appearing peaks at 1095 and 1221 cm^{-1} indicated the C−O−C stretching vibrations. The possible low intensities of C=C peaks referred to the formation of amorphous carbon, as confirmed by the XRD analysis after the carbonization step. Moreover, the increase in intensity of the C−O bond referred to the presence of oxygen functional groups, which was found to be consistent with the XPS results, as discussed before.

3.3. High-Pressure H_2 Storage Measurements. The total H_2 adsorption isotherms for the etched CAs obtained at 298 K and in the pressure range of 0−100 bar are illustrated in Figure 10. The total gravimetric and volumetric adsorption isotherms were obtained from the adsorbed film volume at room temperature, which was estimated from the Ono−Kondo model (eqs 8 and 9), as shown in Figure S3 (Supporting Information), as the total pore volume overestimates the uptake.[48] This method allows for the accurate determination of the absolute uptake values of these CA sorbents. It is evident from these isotherms that the double-activated $CA_{T20\text{-}F25\text{-}KOH}$ sample exhibited the highest uptake at room temperature, reaching 2.1 wt % at 100 bar, as shown in Figure 10a. This represents one of the highest values achieved for a porous material under similar conditions,[18,49−51] with the corresponding sample showing an excess uptake of 1.1 wt % at room temperature and 100 bar. Figure S4 in Supporting Information shows the same trend with the excess adsorption isotherms of the etched CA sorbents, demonstrating that the double-activated $CA_{T20\text{-}F25\text{-}KOH}$ achieved the highest uptake at about 1.6 wt %. Furthermore, the initial total uptake up to 30 bar for the three sorbents followed an increasing order, with values of 0.54 wt % for $CA_{T20\text{-}F50}$, 0.63 wt % for $CA_{T20\text{-}F25}$, and 0.77 wt % for $CA_{T20\text{-}F25\text{-}KOH}$. This exceptionally high uptake at the low-pressure region was attributed to the presence of ultramicropores and the positive influence of oxygen functional groups on the surface. The significant impact of oxygen as an active center was evident when comparing $CA_{T20\text{-}F25}$ and $CA_{T20\text{-}F50}$, resulting in an approximate 17% enhancement in the overall uptake at low pressure. Though $CA_{T20\text{-}F25\text{-}KOH}$ exhibited a decrease of 2.8% O_2 content with respect to $CA_{T20\text{-}F25}$ (Table S1), the synergistic effect of factors such as surface area, total pore volume, and the availability of oxygen binding sites resulted in the enhancement of H_2 uptake compared to $CA_{T20\text{-}F25}$.[8] While the CA sorbents exhibited an impressively high gravimetric uptake, surpassing values reported in existing literature,[36,52] the low bulk density of the aerogels gave rise to a relatively modest volumetric uptake, with $CA_{T20\text{-}F25\text{-}KOH}$ at approximately 6.8 g/L, $CA_{T20\text{-}F25}$ at about 5.4 g/L, and $CA_{T20\text{-}F50}$ at roughly 4.6 g/L, as shown in Figure 10b. The overlap of both adsorption and desorption isotherms without hysteresis indicated complete reversibility of the storage capacity of the sorbents, as evident from Figure S5, Supporting Information.

The total gravimetric and volumetric adsorption isotherms obtained at 77 K and in the 0−100 bar pressure range for CA sorbents are shown in Figure 11. These data were obtained as

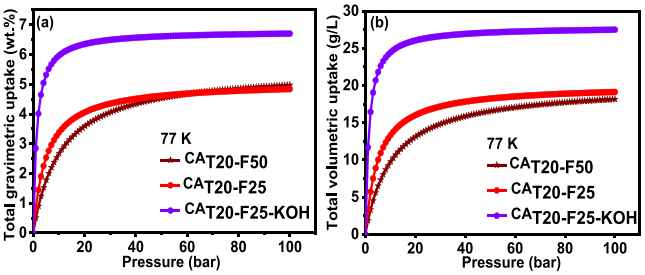

Figure 11. (a) Total gravimetric and (b) volumetric H_2 adsorption isotherms of CA at 77 K and 0−100 bar.

part of an evaluation for a cryo-adsorption-based system designed for vehicular H_2 storage. We noted that the H_2 uptake at 1 bar was in the range of 0.5−3.3 wt % and attributed the high uptake at initial pressure to the combined effect of high ultramicropore surface area and the oxygen-rich surface. This scenario was similar to the high uptake at lower pressure for the sample CA-4700 at 3.9 wt %.[8] Additionally, the oxygen functional groups can act as active centers and can enhance the affinity, making it more effective for low-pressure H_2 storage. At 1 bar, the sample $CA_{T20\text{-}F25\text{-}KOH}$ exhibited the highest uptake of 3.3 wt %, followed by $CA_{T20\text{-}F25}$ at 1.22 wt %, and decreasing to 0.63 wt % for the $CA_{T20\text{-}F50}$ sample.

In order to ascertain the positive influence of an oxygen-rich surface, it is necessary to conduct a comparison between $CA_{T20\text{-}F25}$ and $CA_{T20\text{-}F50}$. These two sorbents share a similar level of porosity, including total surface area, micropore surface area, and ultramicropore volume. The total surface area for both sorbents fall within the range of 2947 m^2/g, with a micropore surface area of 2100 m^2/g and an ultramicropore volume of 1.06 cm^3/g. The slight variation between these values is within approximately ±7%, indicating that their porosity is comparable. The primary distinguishing factor between these two sorbents lies in their oxygen content. $CA_{T20\text{-}F25}$ exhibits a significantly higher oxygen content of 21%, whereas $CA_{T20\text{-}F50}$ contains only 4.5% oxygen. Under 1 bar pressure conditions, $CA_{T20\text{-}F25}$ demonstrated a H_2 storage capacity of 1.22 wt %, which represents a remarkable 50%

https://doi.org/10.1021/acs.chemmater.4c00352
Chem. Mater. 2024, 36, 8565−8577

increase when compared to the 0.63 wt % observed in $CA_{T20\text{-}F50}$. For $CA_{T20\text{-}F25\text{-}KOH}$ at 1 bar, the positive effect of having significantly high ultramicropore volume and oxygen-rich surface enhanced the steep rise in uptake. It was previousely reported that a similar phenomenon of having oxygen-rich surface enhanced the initial uptake at 77 K up to 3.9 wt % for sample CA-4700.[8] Although the sample $CA_{T20\text{-}F25\text{-}KOH}$ boasts a high ultramicropore volume and an oxygen-rich surface, the total gas uptake at high pressure was significantly influenced by the overall surface area and total pore volume via space filling mechanism. Specifically, at 100 bar, $CA_{T20\text{-}F25\text{-}KOH}$ demonstrated the highest uptake at 6.8 wt %, surpassing the DOE target, in contrast to $CA_{T20\text{-}F50}$ with 5.0 wt % and $CA_{T20\text{-}F25}$ with 4.9 wt %. The relatively modest increase in gas uptake at high pressure for $CA_{T20\text{-}F50}$ can be attributed to the slight difference in the available overall surface area, as evident in Figure 11a.

The most notable reported uptakes to date include 8.9 wt % for CA-4700,[8] 7.03 wt % for polypyrrole-based carbons,[50] 7.3 wt % for zeolite-templated carbon, and 5.9 wt % for AX21 (commercially activated carbon).[3] These values are in the same range as the achieved uptake of 6.8 wt % for the double-activated $CA_{T20\text{-}F25\text{-}KOH}$, considering the measurement conditions used. While possessing remarkable gravimetric capacity, the volumetric H_2 uptake of the carbons was assessed considering the sample's bulk density, as shown in Figure 11b. Due to the high porosity nature of the aerogels, the $CA_{T20\text{-}F50}$, $CA_{T20\text{-}F25}$, and $CA_{T20\text{-}F25\text{-}KOH}$ exhibited a low bulk density within the range of 0.21 g/cm^3, consequently reducing the overall volumetric capacity on the order of 28.0 g/L for $CA_{T20\text{-}F25\text{-}KOH}$, 19.4 g/L for $CA_{T20\text{-}F25}$, and 17.9 g/L for $CA_{T20\text{-}F50}$. The double-activated $CA_{T20\text{-}F25\text{-}KOH}$ exhibited an uptake of 3.2 wt % and 13 g/L during pressure-swing delivery (from 100 to 5 bar at 77 K), specifically in terms of working capacity. However, the significant rise in uptake at lower pressure values notably reduced the overall working capacity. In comparison, $CA_{T20\text{-}F50}$ exhibited working capacities of 3.1 wt % and 11.5 g/L, while $CA_{T20\text{-}F25}$ demonstrated capacities of 2.6 wt %, 9.4 g/L, as outlined in Table 4. The discrepancy between initial and overall uptakes profoundly impacted the working capacities of CA sorbents. Strategies to improve this capacity encompass optimizing pore structure, altering surface functionalities, optimizing activation processes, exploring hybrid material designs, and utilizing advanced modeling techniques. These approaches aim to tackle the rapid saturation in initial uptake, potentially extending and maximizing the working capacity of CAs for efficient gas storage applications.

Table 4. H_2 Adsorption Data for Activated Carbons at 77 and 298 K

sorbent	298 K (100 bar)		77 K (100 bar)		working capacity (77 K/100-5 bar)	
	wt %	g/L	wt %	g/L	wt %	g/L
$CA_{T20\text{-}F50}$	1.4	4.6	5.0	17.9	3.1	11.5
$CA_{T20\text{-}F25}$	1.7	5.4	4.9	19.4	2.6	9.4
$CA_{T20\text{-}F25\text{-}KOH}$	2.1	6.8	6.8	28.0	3.2	13

3.4. Cryogenic Determination of Adsorbed Film Density. The adsorbed film volume is difficult to determine through adsorption isotherm at room temperature as the saturation occurs at very high pressures (350−700 bar). Hence, cryogenic adsorption isotherm was adopted to obtain the adsorbed film volume at saturation $\rho_{film,sat}$.[48] At high pressure, the film density saturated to obtain the film volume and the excess isotherm exhibited a linear decay with gas density reaching up to 100 g/L higher than the liquid H_2 density (71 g/L),[48] as defined in eq 8. In the saturation regime, the slope of the isotherm yielded the film volume and the extrapolation to where the isotherm crosses ($G_{ex(\rho film,sat)} = 0$) at $\rho_{film,sat}$ = 100 ± 20 g/L. The data fitted well with the assumptions based on the Ono-Kondo adsorption model (eq 9) and showed the extrapolated maximum at the high-density regime, as evident in Figure 12. With the fit, V_{film} was calculated from the slope of the high-density regime, as given in Table 5.

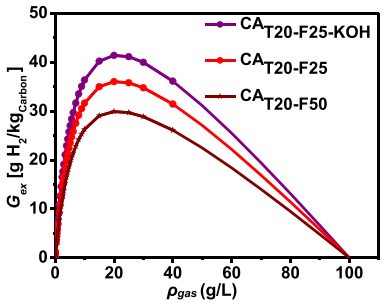

Figure 12. G_{ex} vs ρ_{gas} across 77 K to estimate the adsorbed film volume using the Ono−Kondo model fit.

Table 5. Calculated Adsorbed Film Volume and the Ratio of Film Volume to Pore Volume at 77 K for CA Sorbents Based on the High-Density Regime, $\rho_{film,sat}$ = 100 g/L

sorbent	E_b (kJ/mol)	R^2	V_{film} (cm^3/g)	V_{film}/V_{pore}
$CA_{T20\text{-}F50}$	8.9	0.98	0.20	0.22
$CA_{T20\text{-}F25}$	10.2	0.98	0.32	0.31
$CA_{T20\text{-}F25\text{-}KOH}$	11.3	0.99	0.55	0.40

For the $CA_{T20\text{-}F25\text{-}KOH}$ sample, the calculated V_{film} was 0.55 cm^3/g, which was 40% of the total pore volume obtained at cryogenic temperature. It was followed by $CA_{T20\text{-}F25}$ (V_{film} = 0.32 cm^3/g) and $CA_{T20\text{-}F25}$ (V_{film} = 0.20 cm^3/g) with respect to the availability of bonding sites associated with the narrow pores. The same trend applies to the fitted binding energy (E_b) value at the highest at 11.3 kJ/mol for $CA_{T20\text{-}F25\text{-}KOH}$. Thus, the fit to the model was satisfied with respect to the uncertainty of G_{ex} estimation based on pore volume. The as-obtained film volume was further used in the calculation of the Q_{st}, as shown in Figure 13.

The strength of interactions between adsorbed H_2 molecules and carbon was assessed through the Q_{st}. This parameter was determined by analyzing the absolute adsorption isotherms obtained at three different temperatures: 25, 40, and 55 °C, as shown in Figure S6 in the Supporting Information. Consequently, the Q_{st} for the CA sorbents was derived using the Clausius−Clapeyron equation, as given in eq 10. The absolute heat of adsorption was then computed based on the estimated film volume, as illustrated in Figure 13.

For $CA_{T20\text{-}F25\text{-}KOH}$, the Q_{st} value exhibited variation, starting at 11.3 kJ/mol at low coverage and gradually decreasing to nearly 8.9 kJ/mol at 2 wt %. The initially high value at zero coverage is attributed to the ultramicroporosity and the oxygen-rich binding sites on the surface, with subsequent

https://doi.org/10.1021/acs.chemmater.4c00352
Chem. Mater. 2024, 36, 8565−8577

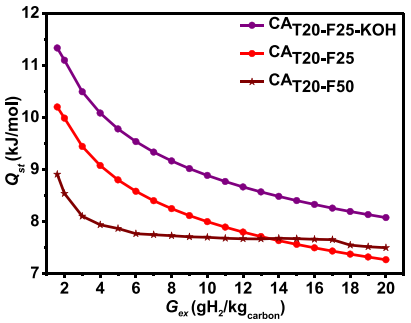

Figure 13. Estimated Q_{st} as a function of excess H_2 uptake (G_{ex}) for CA sorbents.

decreases reflecting the influence of available surface area at higher pressures. Similar values can be found in the literature, where computational studies on carbons with slit-pore geometry indicate these as the strongest binding sites.[54] In the case of $CA_{T20-F25}$, the Q_{st} value stands at 10.2 kJ/mol at zero coverage, indicating moderate microporosity and substantial oxygen-rich binding sites. This value significantly dropped to 7.2 kJ/mol at 2 wt %. $CA_{T20-F50}$ exhibited the lowest Q_{st} values, ranging from 8.9 kJ/mol, gradually decreasing to almost 7.4 kJ/mol at 2 wt % H_2 uptake. Notably, at high coverage, $CA_{T20-F50}$ displayed a Q_{st} value of 7.4 kJ/mol, surpassing $CA_{T20-F25}$ at 7.2 kJ/mol, which can be attributed to its higher surface area. It is worth mentioning here that the elevated Q_{st} values obtained at zero coverage in this study significantly exceed those observed in carbide-derived,[55,56] biomass-derived,[8] and zeolite-templated carbon[18] with comparable levels of microporosity, reaching an average of 10.6 kJ/mol at zero coverage.

Notably, if a storage system is designed not to reduce the material capacity by 20%, $CA_{T20-F25-KOH}$ would have surpassed the 2025 DOE gravimetric system target of 5.5 wt %, as presented in Figure 14. It is also noteworthy that this sorbent is

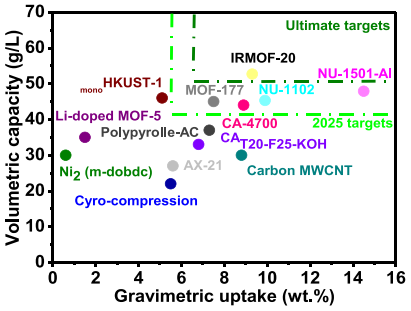

Figure 14. Evaluation of DOE target adherence in relation to both gravimetric and volumetric capacities among benchmark sorbents.

on par with other high-performing benchmark materials including CA-4700,[8] polypyrrole-based activated carbon,[7] AX21,[57] and carbon MWCNT[58] from the existing literature. However, given that packing density plays a crucial role in overall volumetric uptake, achieving a balance between porosity and bulk density is essential to meet DOE target metrics on both gravimetric and volumetric bases. Despite the inherently low bulk density of aerogels, techniques such as pressure compaction,[20] hydrothermal pressing,[59] and CIP[53] into pellets, and direct ink writing (DIW) into monolith formation,[60] with minimal microstructural deformation, can effectively enhance the packing density of these highly porous carbons.

4. CONCLUSIONS

In summary, the investigation of H_2 storage onto etched CA revealed significant insights into the material's performance under various conditions. The results presented emphasized the critical role of optimizing pyrolysis conditions such as residence time and gas flow rate during the etching reaction to achieve the desired high surface area and porosity in aerogels. The total H_2 adsorption isotherms conducted at 298 K and in the pressure range of 0−100 bar demonstrated that the double-activated $CA_{T20-F25-KOH}$ exhibited the highest uptake reaching 2.1 wt % at 298 K and 100 bar pressure. This high uptake at 298 K was attributed to the synergistic effect of oxygen functional groups on the surface and high ultramicropore volume which significantly enhance H_2 adsorption even at room temperature. At 77 K, $CA_{T20-F25}$, with a higher oxygen content, exhibited a 41% increase in gas storage capacity under 1 bar pressure when compared to $CA_{T20-F50}$, emphasizing the significance of surface oxygen groups as active centers. At higher pressures, $CA_{T20-F25-KOH}$ surpassed the 2025 DOE gravimetric system target of 5.5 wt % by achieving 6.8 wt % at 77 K and 100 bar (if a complete storage system designed that does not reduce the material capacity by 20%), outperforming $CA_{T20-F25}$ and $CA_{T20-F50}$. The relatively modest increase in the H_2 uptake for $CA_{T20-F50}$ at high pressure was attributed to a slight difference in overall surface area. The Q_{st} values further reflected the ultramicroporosity and oxygen-rich surface, with $CA_{T20-F25-KOH}$ demonstrating a higher Q_{st} value of 11.3 kJ/mol at zero coverage compared to other carbons reported in the literature. However, striking a balance between porosity and bulk density remains imperative for meeting the DOE system targets on both gravimetric and volumetric bases. This objective is set for future investigation in optimizing the $CA_{T20-F25-KOH}$ sample to achieve increased volumetric capacity. These findings contribute valuable insights into the design and optimization of aerogels for enhanced H_2 adsorption, with implications for the development of high-performance materials in diverse applications.

■ ASSOCIATED CONTENT

Supporting Information

The Supporting Information is available free of charge at https://pubs.acs.org/doi/10.1021/acs.chemmater.4c00352.

N_2 physisorption isotherms, PSD profiles, Ono−Kondo model at 298 K, excess and total H_2 adsorption isotherms at 298 K, XPS elemental composition, and total gravimetric adsorption isotherms at 298, 313, and 328 K for CA-sorbents (PDF)

■ AUTHOR INFORMATION

Corresponding Author

Fateme Rezaei − *Department of Chemical, Environmental and Materials Engineering, University of Miami, Coral Gables, Florida 33124-6914, United States;* orcid.org/0000-0002-4214-4235; Email: rezaeif@miami.edu

Authors

Ruthradharshini Murugavel − *Department of Chemical, Environmental and Materials Engineering, University of Miami, Coral Gables, Florida 33124-6914, United States*

https://doi.org/10.1021/acs.chemmater.4c00352
Chem. Mater. 2024, 36, 8565−8577

Ali A. Rownaghi − *National Energy Technology Laboratory (NETL), United States Department of Energy, Pittsburgh, Pennsylvania 15236-0940, United States;* orcid.org/0000-0001-5228-5624

Complete contact information is available at: https://pubs.acs.org/10.1021/acs.chemmater.4c00352

Notes

The authors declare no competing financial interest.

■ ACKNOWLEDGMENTS

We sincerely thank the National Science Foundation (NSF PFI-2044726) for financial support.

■ REFERENCES

(1) Meneghelli, B.; Tamburello, D.; Fesmire, J.; Swanger, A. *Integrated Insulation System for Automotive Cryogenic*; U.S. DOE Hydrogen and Fuel Cells Program, 2017.

(2) Murugavel, R.; Rownaghi, A. A.; Rezaei, F. Effect of Alkali Metal Functionalization on Hydrogen Storage Performance of Highly Porous Activated Carbons. *Energy & Fuels* **2023**, *37*, 19292.

(3) Poirier, E.; Chahine, R.; Bose, T. K. Hydrogen Adsorption in Carbon Nanostructures. *Int. J. Hydrogen Energy* **2001**, *26* (8), 831−835.

(4) Pham, T. D.; Sengupta, D.; Farha, O. K.; Snurr, R. Q. Investigation of Anionic Metal−Organic Frameworks with Extra-Framework Cations for Room Temperature Hydrogen Storage. *Chem. Mater.* **2024**, *36* (8), 3794−3802.

(5) Al-Naddaf, Q.; Al-Mansour, M.; Thakkar, H.; Rezaei, F. MOF-GO Hybrid Nanocomposite Adsorbents for Methane Storage. *Ind. Eng. Chem. Res.* **2018**, *57* (51), 17470−17479.

(6) Zhang, X.; Liu, Y.; Ren, Z.; Zhang, X.; Hu, J.; Huang, Z.; Lu, Y.; Gao, M.; Pan, H. Realizing 6.7 Wt% Reversible Storage of Hydrogen at Ambient Temperature with Non-Confined Ultrafine Magnesium Hydrides. *Energy Environ. Sci.* **2021**, *14* (4), 2302−2313.

(7) Sevilla, M.; Mokaya, R.; Fuertes, A. B. Ultrahigh Surface Area Polypyrrole-Based Carbons with Superior Performance for Hydrogen Storage. *Energy Environ. Sci.* **2011**, *4* (8), 2930−2936.

(8) Blankenship, T. S.; Balahmar, N.; Mokaya, R. Oxygen-Rich Microporous Carbons with Exceptional Hydrogen Storage Capacity. *Nat. Commun.* **2017**, *8* (1), 1545 DOI: 10.1038/s41467-017-01633-x.

(9) Liu, C.; Fan, Y. Y.; Liu, M.; Cong, H. T.; Cheng, H. M.; Dresselhaus, M. S. Hydrogen Storage in Single-Walled Carbon Nanotubes at Room Temperature. *Science (1979)* **1999**, *286* (5442), 1127−1129.

(10) Froudakis, G. E. Why Alkali-Metal-Doped Carbon Nanotubes Possess High Hydrogen Uptake. *Nano Lett.* **2001**, *1* (10), 531−533.

(11) Chen, P.; Wu, X.; Lin, J.; Tan, K. L. High H2 Uptake by Alkali-Doped Carbon Nanotubes Under Ambient Pressure and Moderate Temperatures. *Science (1979)* **1999**, *285* (5424), 91−93.

(12) Arkook, B.; Alshahrie, A.; Salah, N.; Aslam, M.; Aissan, S.; Al-Ojeery, A.; Al-Ghamdi, A.; Inoue, A.; Shalaan, E.-S. Graphene and Carbon Nanotubes Fibrous Composite Decorated with PdMg Alloy Nanoparticles with Enhanced Absorption−Desorption Kinetics for Hydrogen Storage Application. *Nanomaterials* **2021**, *11* (11). 2957.

(13) Al-Naddaf, Q.; Majedi Far, H.; Cheshomi, N.; Rownaghi, A. A.; Rezaei, F. Exceptionally High Gravimetric Methane Storage in Aerogel-Derived Carbons. *Ind. Eng. Chem. Res.* **2020**, *59* (43), 19383−19391.

(14) Alwin, S.; Sahaya Shajan, X. Aerogels: Promising Nano-structured Materials for Energy Conversion and Storage Applications. *Mater. Renew Sustain Energy* **2020**, *9* (2), 7.

(15) Pekala, R. W. Organic Aerogels from the Polycondensation of Resorcinol with Formaldehyde. *J. Mater. Sci.* **1989**, *24* (9), 3221−3227.

(16) Vergara-Rubio, A.; Ribba, L.; Picón Borregales, D. E.; Sapag, K.; Candal, R.; Goyanes, S. Ultramicroporous Carbon Nanofibrous Mats for Hydrogen Storage. *ACS Appl. Nano Mater.* **2022**, *5* (10), 15353−15361.

(17) Suarez-Garcia, F.; Vilaplana-Ortego, E.; Kunowsky, M.; Kimura, M.; Oya, A.; Linares-Solano, A. Activation of Polymer Blend Carbon Nanofibres by Alkaline Hydroxides and Their Hydrogen Storage Performances. *Int. J. Hydrogen Energy* **2009**, *34* (22), 9141−9150.

(18) Nishihara, H.; Hou, P.-X.; Li, L.-X.; Ito, M.; Uchiyama, M.; Kaburagi, T.; Ikura, A.; Katamura, J.; Kawarada, T.; Mizuuchi, K.; Kyotani, T. High-Pressure Hydrogen Storage in Zeolite-Templated Carbon. *J. Phys. Chem. C* **2009**, *113* (8), 3189−3196.

(19) Yang, Z.; Xia, Y.; Mokaya, R. Enhanced Hydrogen Storage Capacity of High Surface Area Zeolite-like Carbon Materials. *J. Am. Chem. Soc.* **2007**, *129* (6), 1673−1679.

(20) Masika, E.; Mokaya, R. Exceptional Gravimetric and Volumetric Hydrogen Storage for Densified Zeolite Templated Carbons with High Mechanical Stability. *Energy Environ. Sci.* **2014**, *7* (1), 427−434.

(21) Cousins, K.; Zhang, R. Highly Porous Organic Polymers for Hydrogen Fuel Storage. *Polymers (Basel)* **2019**, *11* (4). 690.

(22) Kostoglou, N.; Koczwara, C.; Stock, S.; Tampaxis, C.; Charalambopoulou, G.; Steriotis, T.; Paris, O.; Rebholz, C.; Mitterer, C. Nanoporous Polymer-Derived Activated Carbon for Hydrogen Adsorption and Electrochemical Energy Storage. *Chemical Engineering Journal* **2022**, *427*, No. 131730.

(23) Liu, S.; Sui, Z.-Y.; Wang, T.-X.; Zhou, H.-Y.; Liu, Y.-W.; Han, B.-H. Tuning Both Surface Chemistry and Porous Properties of Polymer-Derived Porous Carbons for High-Performance Gas Adsorption. *Langmuir* **2019**, *35* (24), 7650−7658.

(24) Chung, T. C. M.; Jeong, Y.; Chen, Q.; Kleinhammes, A.; Wu, Y. Synthesis of Microporous Boron-Substituted Carbon (B/C) Materials Using Polymeric Precursors for Hydrogen Physisorption. *J. Am. Chem. Soc.* **2008**, *130* (21), 6668−6669.

(25) Pandey, A. P.; Bhatnagar, A.; Shukla, V.; Soni, P. K.; Singh, S.; Verma, S. K.; Shaneeth, M.; Sekkar, V.; Srivastava, O. N. Hydrogen Storage Properties of Carbon Aerogel Synthesized by Ambient Pressure Drying Using New Catalyst Triethylamine. *Int. J. Hydrogen Energy* **2020**, *45* (55), 30818−30827.

(26) Gogotsi, Y.; Portet, C.; Osswald, S.; Simmons, J. M.; Yildirim, T.; Laudisio, G.; Fischer, J. E. Importance of Pore Size in High-Pressure Hydrogen Storage by Porous Carbons. *Int. J. Hydrogen Energy* **2009**, *34* (15), 6314−6319.

(27) Far, H. M.; Lawson, S.; Al-Naddaf, Q.; Rezaei, F.; Sotiriou-Leventis, C.; Rownaghi, A. A. Advanced Pore Characterization and Adsorption of Light Gases over Aerogel-Derived Activated Carbon. *Microporous Mesoporous Mater.* **2021**, *313*, No. 110833.

(28) Román, S.; González, J. F.; González-García, C. M.; Zamora, F. Control of Pore Development during CO_2 and Steam Activation of Olive Stones. *Fuel Process. Technol.* **2008**, *89* (8), 715−720.

(29) González, M. T.; Rodríguez-Reinoso, F.; García, A. N.; Marcilla, A. CO2 Activation of Olive Stones Carbonized under Different Experimental Conditions. *Carbon N Y* **1997**, *35* (1), 159−162.

(30) Javed, M.; Zahoor, M.; Mazari, S. A.; Qureshi, S. S.; Sabzoi, N.; Jatoi, A. S.; Mubarak, N. M. An Overview of Effect of Process Parameters for Removal of CO_2 Using Biomass-Derived Adsorbents. *Biomass Convers Biorefin* **2023**, *13* (6), 4495−4513.

(31) Nair, C. P. R. Advances in Addition-Cure Phenolic Resins. *Prog. Polym. Sci.* **2004**, *29* (5), 401−498.

(32) Far, H. M.; Donthula, S.; Taghvaee, T.; Saeed, A. M.; Garr, Z.; Sotiriou-Leventis, C.; Leventis, N. Air-Oxidation of Phenolic Resin Aerogels: Backbone Reorganization, Formation of Ring-Fused Pyrylium Cations, and the Effect on Microporous Carbons with Enhanced Surface Areas. *RSC Adv.* **2017**, *7* (81), 51104−51120.

(33) Lemmon, E. W. Thermophysical Properties of Fluid Systems. In *NIST Chemistry WebBook, NIST Standard Reference Database Number 69*; National Institute of Standards and Technology, 2005.

(34) Hirscher, M.; Zhang, L.; Oh, H. Nanoporous Adsorbents for Hydrogen Storage. *Appl. Phys. A: Mater. Sci. Process.* **2023**, *129* (2), 112.

(35) Thommes, M.; Kaneko, K.; Neimark, A. V.; Olivier, J. P.; Rodriguez-Reinoso, F.; Rouquerol, J.; Sing, K. S. W. Physisorption of Gases, with Special Reference to the Evaluation of Surface Area and Pore Size Distribution (IUPAC Technical Report). *Pure Appl. Chem.* **2015**, *87* (9−10), 1051−1069.
(36) Jordá-Beneyto, M.; Suárez-García, F.; Lozano-Castelló, D.; Cazorla-Amorós, D.; Linares-Solano, A. Hydrogen Storage on Chemically Activated Carbons and Carbon Nanomaterials at High Pressures. *Carbon N Y* **2007**, *45* (2), 293−303.
(37) Chang, C.-F.; Chang, C.-Y.; Tsai, W.-T. Effects of Burn-off and Activation Temperature on Preparation of Activated Carbon from Corn Cob Agrowaste by CO_2 and Steam. *J. Colloid Interface Sci.* **2000**, *232* (1), 45−49.
(38) Gao, F.; Zhao, D.-L.; Li, Y.; Li, X.-G. Preparation and Hydrogen Storage of Activated Rayon-Based Carbon Fibers with High Specific Surface Area. *J. Phys. Chem. Solids* **2010**, *71* (4), 444−447.
(39) Liu, X.; Zhang, C.; Geng, Z.; Cai, M. High-Pressure Hydrogen Storage and Optimizing Fabrication of Corncob-Derived Activated Carbon. *Microporous Mesoporous Mater.* **2014**, *194*, 60−65.
(40) Coromina, H. M.; Walsh, D. A.; Mokaya, R. Biomass-Derived Activated Carbon with Simultaneously Enhanced CO_2 Uptake for Both Pre and Post Combustion Capture Applications. *J. Mater. Chem. A* **2016**, *4* (1), 280−289.
(41) Caturla, F.; Molina-Sabio, M.; Rodríguez-Reinoso, F. Preparation of Activated Carbon by Chemical Activation with $ZnCl_2$. *Carbon N Y* **1991**, *29* (7), 999−1007.
(42) Molina-Sabio, M.; Rodríguez-Reinoso, F. Role of Chemical Activation in the Development of Carbon Porosity. *Colloids Surf. A Physicochem Eng. Asp* **2004**, *241* (1), 15−25.
(43) Rouquerol, F.; Rouquerol, J.; Sing, K. CHAPTER 6 - Assessment of Surface Area. In *Adsorption by Powders and Porous Solids*; Rouquerol, F.; Rouquerol, J.; Sing, K., Eds.; Academic Press: London, 1999; pp 165−189.
(44) Yu, P.; Luo, Z.; Wang, Q.; Fang, M.; Zhou, J.; Wang, W.; Liang, X.; Cai, W. Activated Carbon-Based CO_2 Uptake Evaluation at Different Temperatures: The Correlation Analysis and Coupling Effects of the Preparation Conditions. *Journal of CO2 Utilization* **2020**, *40*, No. 101214.
(45) Yoon, Y. H.; O'Nolan, D.; Beauvais, M. L.; Chapman, K. W.; Lively, R. P. Direct Evidence of the Ultramicroporous Structure of Carbon Molecular Sieves. *Carbon N Y* **2023**, *210*, No. 118002.
(46) Kumar, V.; Kumar, A.; Lee, D.-J.; Park, S.-S. Estimation of Number of Graphene Layers Using Different Methods: A Focused Review. *Materials* **2021**, *14* (16), 4590.
(47) Wang, Z.; Yang, F. H.; Yang, R. T. Enhanced Hydrogen Spillover on Carbon Surfaces Modified by Oxygen Plasma. *J. Phys. Chem. C* **2010**, *114* (3), 1601−1609.
(48) Knight, E. W.; Gillespie, A. K.; Prosniewski, M. J.; Stalla, D.; Dohnke, E.; Rash, T. A.; Pfeifer, P.; Wexler, C. Determination of the Enthalpy of Adsorption of Hydrogen in Activated Carbon at Room Temperature. *Int. J. Hydrogen Energy* **2020**, *45* (31), 15541−15552.
(49) Lachawiec, A. J.; Qi, G.; Yang, R. T. Hydrogen Storage in Nanostructured Carbons by Spillover: Bridge-Building Enhancement. *Langmuir* **2005**, *21* (24), 11418−11424.
(50) Adeniran, B.; Mokaya, R. Compactivation: A Mechanochemical Approach to Carbons with Superior Porosity and Exceptional Performance for Hydrogen and CO_2 Storage. *Nano Energy* **2015**, *16*, 173−185.
(51) Stadie, N. P.; Vajo, J. J.; Cumberland, R. W.; Wilson, A. A.; Ahn, C. C.; Fultz, B. Zeolite-Templated Carbon Materials for High-Pressure Hydrogen Storage. *Langmuir* **2012**, *28* (26), 10057−10063.
(52) Wang, H.; Gao, Q.; Hu, J. High Hydrogen Storage Capacity of Porous Carbons Prepared by Using Activated Carbon. *J. Am. Chem. Soc.* **2009**, *131* (20), 7016−7022.
(53) Li, H.; Komatsu, K.; Tsuda, Y.; Saitoh, H. Hydrogen Adsorption with Micro-Structure Deformation in Nanoporous Carbon under Ultra-High Pressure. *Int. J. Hydrogen Energy* **2022**, *47* (81), 34555−34569.
(54) Rzepka, M.; Lamp, P.; de la Casa-Lillo, M. A. Physisorption of Hydrogen on Microporous Carbon and Carbon Nanotubes. *J. Phys. Chem. B* **1998**, *102* (52), 10894−10898.
(55) Sevilla, M.; Foulston, R.; Mokaya, R. Superactivated Carbide-Derived Carbons with High Hydrogen Storage Capacity. *Energy Environ. Sci.* **2010**, *3* (2), 223−227.
(56) Yushin, G.; Dash, R.; Jagiello, J.; Fischer, J. E.; Gogotsi, Y. Carbide-Derived Carbons: Effect of Pore Size on Hydrogen Uptake and Heat of Adsorption. *Adv. Funct Mater.* **2006**, *16* (17), 2288−2293.
(57) Bénard, P.; Chahine, R. Determination of the Adsorption Isotherms of Hydrogen on Activated Carbons above the Critical Temperature of the Adsorbate over Wide Temperature and Pressure Ranges. *Langmuir* **2001**, *17* (6), 1950−1955.
(58) Biehler, E.; Quach, Q.; Abdel-Fattah, T. M. Screening Study of Different Carbon-Based Materials for Hydrogen Storage. *ECS J. Solid State Sci. Technol.* **2023**, *12* (8), No. 081002.
(59) Sariyev, B.; Abdikadyr, A.; Baitikenov, T.; Anuarbekov, Y.; Golman, B.; Spitas, C. Thermal Properties and Mechanical Behavior of Hot Pressed PEEK/Graphite Thin Film Laminate Composites. *Sci. Rep* **2023**, *13* (1), 12785.
(60) Lawson, S.; Al-Naddaf, Q.; Newport, K.; Rownaghi, A.; Rezaei, F. Assessment of CO_2/CH_4 Separation Performance of 3D-Printed Carbon Monoliths in Pressure Swing Adsorption. *Ind. Eng. Chem. Res.* **2021**, *60* (45), 16445−16456.

https://doi.org/10.1021/acs.chemmater.4c00352
Chem. Mater. 2024, 36, 8565−8577